A non-peer-reviewed preprint. Later versions may include revisions and updates.

FluxFormer: Upscaled global gross primary productivity from eddy covariance data with MVTS Transformer model and global ESA-CCI PFT dataset v2.0.8

Anh Phan [1], **Hiromichi Fukui** [1,2]

[1]Chubu Institute for Advanced Studies, Chubu University, Kasugai, Japan
[2]International Digital Earth Applied Science Research Center (IDEAS), Chubu University, Kasugai, Japan

Key Points:

- We evaluate the architecture, optimal sequence length, and PFT dataset selection of a data-driven model to improve GPP prediction accuracy
- We introduce FluxFormer, a framework and global dataset optimizing GPP estimates from 2001 to 2020 at a 0.1-degree spatial resolution
- FluxFormer performs well in evaluations against flux site data and other upscaled datasets, showing promising results

Corresponding author: Anh Phan, `anhphancu@gmail.com`

Abstract

Accurate terrestrial gross primary productivity (GPP) estimates are crucial for developing effective climate change policies. However, quantifying GPP is challenging due to sparse ground observations and the complexity of plant functional types (PFTs). In this study, we address these challenges by evaluating various aspects of a data-driven model, including the architecture of time series deep learning models, the optimal sequence length for input data, and the selection of an appropriate PFT dataset to improve GPP prediction accuracy. We introduce FluxFormer, a comprehensive framework and global dataset designed to optimize GPP estimates from 2001 to 2020 at a 0.1-degree spatial resolution. FluxFormer leverages the updated global PFT dataset v2.0.8 from the ESA Land Cover Climate Change Initiative (ESA-CCI) and combines this with time series remote sensing and climate data using a Multivariate Time Series (MVTS) Transformer model. Our comprehensive evaluations show that FluxFormer's model architecture and optimal sequence length selection significantly improve monthly GPP predictions and their mean seasonal cycle, especially in tropical regions. We also demonstrate that incorporating the ESA-CCI PFT dataset v2.0.8 yields a more reliable GPP dataset compared to using the Moderate Resolution Imaging Spectroradiometer 1D PFT dataset. Additionally, FluxFormer exhibits reduced interannual variability in arid regions and captures a positive long-term GPP trend (2001-2021) consistent with carbon dioxide (CO_2) fertilization effects, an aspect missing in some existing datasets. FluxFormer can thus serve as a tool for refining carbon flux estimates and for cross-verifying datasets.

Plain Language Summary

Terrestrial carbon fluxes, especially gross primary production (the carbon amount fixed by plants through photosynthesis), are pivotal for ecosystem health and the overall carbon balance of the Earth. We present FluxFormer, a data-driven model that generates a monthly global dataset of gross primary production. This dataset is produced using a deep learning model specifically designed for multivariate time series representation learning and updated global plant species information. Through a comprehensive evaluation of FluxFormer, encompassing the choice of input datasets, data-driven model algorithms, and the resulting products, we observed improvements in certain validation metrics, indicating its potential for cross-verifying and enhancing existing datasets.

1 Introduction

Terrestrial ecosystems, acting as a powerful carbon sink, play a crucial role in mitigating global warming (Pan et al., 2011). From 1960 to 2022, this terrestrial sink has outpaced the ocean, offsetting 31% of fossil CO_2 emissions compared to the ocean's projected 25% (Friedlingstein et al., 2023). This vital role is largely driven by terrestrial GPP, a major global carbon flux (Beer et al., 2010), which significantly contributes to terrestrial carbon sequestration.

Estimating terrestrial carbon fluxes, especially GPP, encompasses diverse methods. This includes simulating dynamic global vegetation models (DGVMs) as demonstrated in the TRENDY project (Sitch et al., 2015; Le Quéré et al., 2018), and upscaling from measurements obtained through eddy covariance (EC) flux tower and satellite observations (Jung et al., 2019; Zeng et al., 2020). Despite widespread reliance on PFTs for ecosystem productivity estimates (Poulter et al., 2011, 2015; Lin et al., 2021; Guo et al., 2023; Yan et al., 2023), inconsistencies in PFT data significantly impact GPP and other climate variables at regional and global scales (Poulter et al., 2011).

PFT datasets either provide a 1D or 2D representation of real-world PFT data. 1D data categorize PFTs as discrete types based on the dominant PFT within a pixel area, while 2D data offer a continuous coverage of local PFTs within a pixel area, which is typically used in Earth system and land surface models. The International Geosphere-Biosphere Program (IGBP) classification is a widely used 1D PFT scheme for upscaling GPP from flux site observations. Its popularity is attributed to its well-established nature, ease of access, direct linkage to FLUXNET data (FLUXNET, 2024), and its conceptual simplicity, which facilitates visualization and understanding (Cranko Page et al., 2024). However, despite its common use, the IGBP classification is considered outdated, and relying on it is not recommended for bridging climate inputs to terrestrial fluxes (Cranko Page et al., 2024).

Recent efforts have focused on improving PFT representation, with the latest advancement being the release of the new ESA-CCI PFT dataset v2.0.8 (Harper et al., 2022). Using global land surface model simulations, Harper et al. (2022) assessed the impact of regional updates in the new PFT distribution on climate-related variables, including GPP. For instance, in tropical regions characterized by high tree diversity and complex rainforest structures (Montgomery & Chazdon, 2001), a reduction in tree fraction from the new PFT data leads to a slight increase in albedo, which in turn results in lower evapotranspiration and GPP. However, the effects of the ESA-CCI PFT dataset v2.0.8 on other aspects of derived GPP products, such as interannual variability, mean seasonal cycles, and uncertainty in simulated GPP, need to be thoroughly evaluated, a task that has not yet been addressed in previous studies.

Reliable long-term time series data for both GPP and its predictors are crucial for understanding the physical mechanisms affecting GPP, particularly when using data-driven causal methods, which have recently gained significant attention (Runge et al., 2019; Díaz et al., 2022; Runge et al., 2023). The value of incorporating long-term temporal structures of predictors has been demonstrated (Besnard et al., 2019), highlighting its potential to enhance future GPP upscaled products (Jung et al., 2020). Several attempts have been made to utilize time series predictors with both sequence and non-sequence machine learning models to upscale carbon flux from flux site (Kämäräinen et al., 2023; Nathaniel et al., 2023). However, the optimal choice of data-driven model and the appropriate sequence length for temporal predictors have not yet been fully elucidated. Recently, state-of-the-art deep learning models specifically designed for time series representation learning like MVTS Transformer (Zerveas et al., 2021), Informer (H. Zhou et al., 2021), Autoformer (Wu et al., 2021), and Fedformer (T. Zhou et al., 2022) have been gaining popularity for their ability to capture temporal dynamics and seasonality. While these models hold promise for upscaling global carbon fluxes, their application in this domain remains scarce. Therefore, it is essential to assess the performance of these recent models relative to other approaches and determine the optimal sequence length for temporal predictors in upscaling GPP from flux sites.

In this study, we evaluate the effectiveness of a novel approach that employs an MVTS Transformer model (Zerveas et al., 2021), and the updated ESA-CCI PFT dataset v2.0.8 (Harper et al., 2022), to predict global monthly gross primary production. Our objectives are threefold: First, we assess the performance of the MVTS Transformer in comparison to other popular machine learning and deep learning models and determine the optimal sequence length for time series input data. Second, we investigate the advantages of using the ESA-CCI PFT dataset v2.0.8 over the IGBP PFT data for upscaling GPP. Finally, we compare the generated GPP products — FluxFormer with other satellite-based upscaled datasets, evaluating aspects such as mean annual GPP distribution, interannual variability, and the mean seasonal cycle. The FluxFormer GPP dataset could be used to validate terrestrial biosphere models and serve as a tool for cross-checking other datasets.

2 Data

2.1 FLUXNET 2015

We leveraged FLUXNET 2015 as our reference data (Pastorello et al., 2020), extracting monthly GPP from 206 tier 1 EC sites. The FLUXNET 2015 dataset exhibits an uneven distribution of sites across different climate zones. Notably, tropical and semi-arid regions, despite their significant contributions to both observed GPP values (e.g., Amazonia, Central Africa, Southeast Asia) (M. Chen et al., 2017), and the global carbon cycle (Poulter et al., 2014), are under-represented compared to other areas. The mixed use of open-path and closed-path gas analyzers may contribute to uncertainties and regional biases in the final upscaled product due to differences in their operating principles (Hirata et al., 2007; Burba et al., 2008; Haslwanter et al., 2009). This requires further in-depth analysis in a future study to address and correct these biases.

Following the workflow of data preprocessing pipeline from previous study (Tramontana et al., 2016), we filtered out records with a quality control value below 80% for measured and reliable gap-fill data. Relying solely on quality control values is reported to be insufficient for obtaining qualified data due to inconsistencies in the differences between GPP, ecosystem respiration (RECO), and net ecosystem exchange (NEE) (Zeng et al., 2020; Tramontana et al., 2016). We also filtered out data points with extreme differences based on the computed linear regression values between two flux-partitioning methods for GPP and the difference between GPP-RECO and NEE. Data points with residuals falling outside the range of ± 3 times the interquartile range were excluded. This resulted in a total of 10513 training samples derived from an initial pool of 12094 qualified monthly samples. The distribution of FLUXNET sites is shown in Figure 1, along with the data availability statistic by climate regions and by main IGBP PFTs.

2.2 Remote sensing data

For remote sensing data, we used the Moderate Resolution Imaging Spectroradiometer (MODIS) dataset for leaf area index (LAI) and fraction of absorbed photosynthetic active radiation (FPAR), specifically the MOD15A2H.061 8-day composite dataset available at a 500 m spatial resolution (Myneni et al., 2021), which was collected via Google Earth Engine (Gorelick et al., 2017). For quality control (QC), we selected only the good-quality LAI and FPAR data by filtering the corresponding QC band bit mask included in the MODIS product, which indicates retrievals from the main algorithm with or without saturation. Although previous studies have utilized a range of remote sensing predictors, some incorporating additional variables such as land surface temperature and other vegetation and water indices (Y. Zhang et al., 2017; Tramontana et al., 2016; Jung et al., 2019), and others focusing solely on LAI and FPAR (Zeng et al., 2020; Nathaniel et al., 2023). We chose to use only the most commonly employed and minimal set of predictors, specifically LAI and FPAR.

2.3 ERA5 reanalysis data

In addition to MODIS data, we employed specific variables from the ERA5 reanalysis product (Muñoz Sabater, 2019), including 2-meter air temperature (T2M), surface short-wave (solar) radiation downwards (SSRD), vapor pressure deficit (VPD), total precipitation (TP), and total evaporation (E). As VPD is not directly available in the original dataset, we estimated it using the relationship between saturated vapor pressure (SVP) and actual vapor pressure (AVP): VPD = SVP - AVP, based on T2M and dewpoint temperature. These predictors were selected based on a literature review of previous studies (Tramontana et al., 2016; Jung et al., 2019; Zeng et al., 2020), as well as a recent comparison evaluating the ability of different sets of explanatory variables to predict GPP (Gaber et al., 2024). The original ERA5 data, with a 0.1-degree spatial resolution was

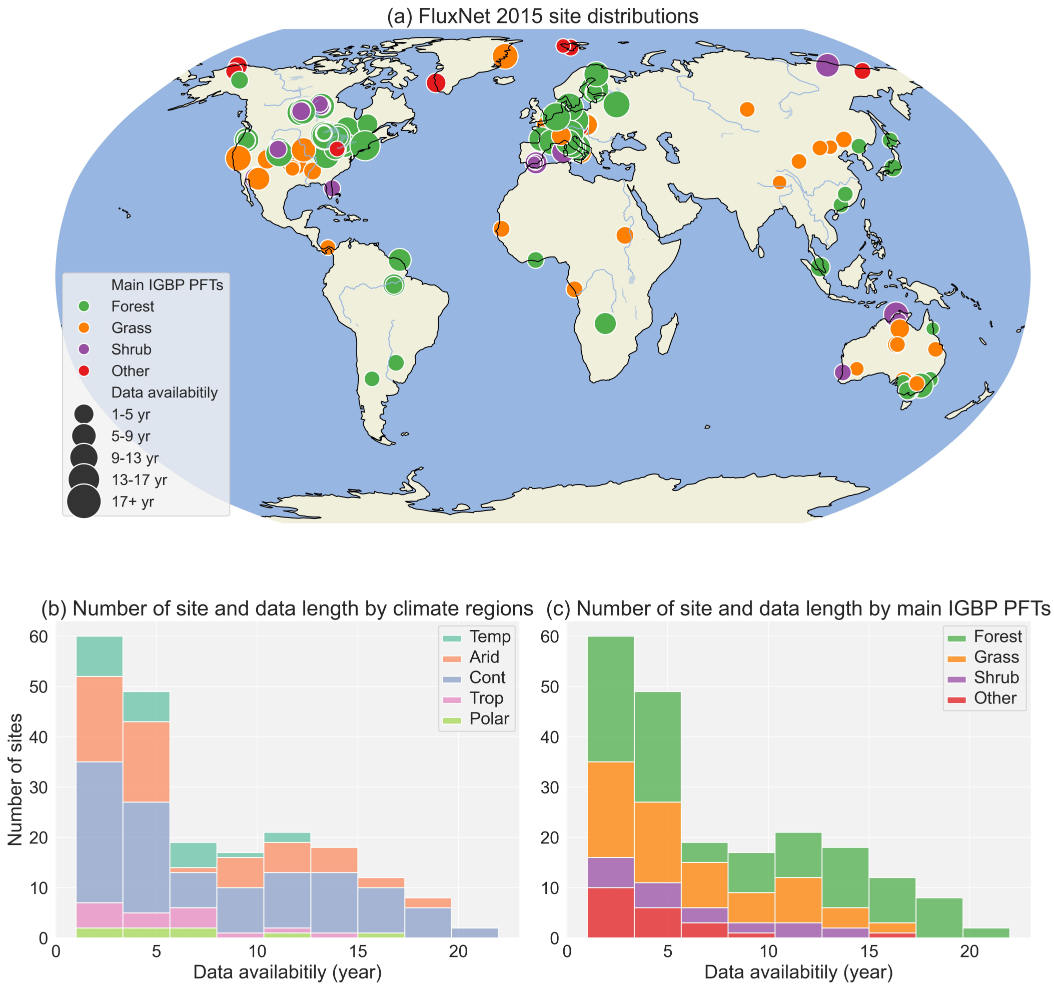

Figure 1. (a) FluxNet 2015 site distributions and data availability statistic by climate region (b) and main IGBP PFTs (c).

obtained from the Copernicus Climate Change Service Climate Data Store (Muñoz Sabater, 2019).

2.4 Plant function types

2.4.1 ESA CCI PFT Data

We leveraged the updated global PFT dataset (PFT v2.0.8) (Harper et al., 2022), spanning 1992-2020. This high-resolution (300m) dataset provides the percentage cover of 14 PFTs for each pixel, offering a more faithful representation of global PFT distributions. Notably, it incorporates high-resolution, peer-reviewed vegetation class mapping, refining global PFT assumptions and potentially impacting regional carbon flux estimates (Harper et al., 2022). The complete set of PFTs includes bare soil, built areas, water bodies, snow and ice, natural grasses, managed grasses, broadleaved deciduous trees, broadleaved evergreen trees, needleleaved deciduous trees, needleleaved evergreen trees, broadleaved deciduous shrubs, broadleaved evergreen shrubs, needleleaved deciduous shrubs, and needleleaved evergreen shrubs.

2.4.2 MODIS IGBP PFT Data

We utilized the PFT information from the MODIS land cover type product MCD12Q1.061, which is available at a spatial resolution of 500 meters (M. Friedl & Sulla-Menashe, 2019). This dataset was accessed through Google Earth Engine (Gorelick et al., 2017). The MODIS product offers global land cover classifications at annual intervals from 2001 to 2020. Specifically, the Land Cover Type 1 product is based on the IGBP classification scheme, which defines 17 distinct land cover classes, assuming that each pixel is 100% covered by a single PFT, an assumption that does not realistically reflect real-world conditions. This dataset was used for comparison with the ESA-CCI PFT dataset in the context of upscaling GPP from flux site data.

3 Method

3.1 Multivariate Time Series Transformer Framework

Figure 2 details the workflow of FluxFormer, our method for upscaling GPP using remote sensing, climate and PFT data. We leverage the MVTS Transformer model (Zerveas et al., 2021), known for its strong performance in multivariate time series regression, even with limited data. Its core components include an input encoding layer with proposed learnable positional encoding and a Transformer encoder. An in-depth introduction of Transformer architecture is presented in (Vaswani et al., 2017), and Zerveas et al. (2021) provides detailed information on learnable positional encoding. Here, we describe the modifications we have implemented to adapt these methods for use with multivariate time series data from remote sensing and climate sources, as well as non-time-series PFT data.

Despite both the ESA-CCI and MODIS-IGBP PFT datasets being time series data available annually (one record per year), their temporal resolution is much coarser than the monthly FLUXNET 2015 data (12 records per year). Therefore, annual PFT data is considered a non-temporal variable (condition/context variable), and it would be inefficient to input it directly through a time series model. Consequently, we modified the original MVTS input encoder to handle the non-time-series context variable from PFT, as shown in Figure 2. We separately encoded the annual PFT classes from each dataset using the same simple encoder consisting of three linear layers. The output vector from each PFT encoder was then concatenated with the projected vector from the time series remote sensing and climate input data.

To train the MVTS Transformer model, we first extracted remote sensing, climate, and PFT data associated with each monthly record from the FLUXNET 2015 dataset. The PFT data was directly input into its corresponding encoder. Since MODIS-IGBP PFT is 1D categorical data, we applied one-hot encoding before feeding it into the encoder.

The extracted remote sensing and climate data was then organized for input into the deep learning model. Specifically, for a given month $\mathbf{M}$, each training sample $\mathbf{X} \in \mathbb{R}^{w \times m}$, where w denotes the length of the time series for month $\mathbf{M}$. The value of w corresponds to the minimum number of 8-day remote sensing records for month $\mathbf{M}$ across all years, ranging from four records in January to 44 records in December. The variable m represents the number of different variables ($m = 7$), which include 7 remote sensing and climate variables from MODIS and ERA5 reanalysis data: LAI, FPAR, T2M, SSRD, VPD, TP, and E. This forms a sequence of w feature vectors $\mathbf{x}_t \in \mathbb{R}^m$, resulting in $\mathbf{X} \in \mathbb{R}^{w \times m} = [\mathbf{x}_1, \mathbf{x}_2, \ldots, \mathbf{x}_w]$. This sequence represents a multivariate time series of length w with m different variables.

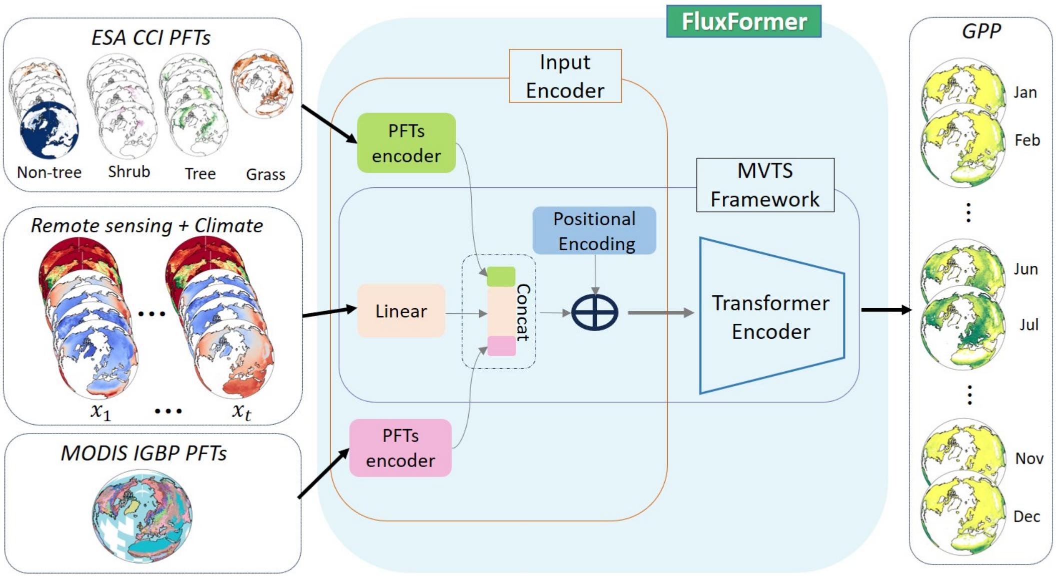

Figure 2. Schematic workflow of our FluxFormer methodology based on remote sensing (RS), climate (ERA5), and PFTs data.

3.2 Validation

To thoroughly evaluate each aspect introduced in this study, we designed three validation experiments as illustrated in Figure 3. First, we examined different model architectures, including both time-series and non-time-series models, in combination with various input sequence lengths and PFT datasets. These models were trained and validated against the ground truth data from FLUXNET 2015. Next, we evaluated the impact of two PFT datasets (ESA-CCI and MODIS-IGBP) on the upscaled GPP products generated from the optimal model configurations. Finally, we created the final upscaled GPP dataset based on the best model and PFT data, and validated it against other widely used upscaled GPP products generated with data-driven and light use efficiency (LUE) models.

3.2.1 Model performance evaluation

To evaluate model performance, we used a five-fold cross-validation scheme to partition the training and validation data. The training data was randomly divided into five groups (folds), with each fold used for testing while the remaining four folds were used for training. We adhered to a specific rule for fold splitting, as recommended by Tramontana et al. (2016); Ichii et al. (2017), which is commonly applied in GPP upscaling models. This rule involves assigning the entire time series from a given site to the same fold, facilitating the assessment of the model's extrapolation capability. For this evaluation, we used Root Mean Square Error (RMSE) and the coefficient of determination (R^2) as the metrics to evaluate the performance of the models in each test case. To evaluate the performance of the proposed model, we conducted comprehensive validation experiments with three main objectives:

We tested the performance of FluxFormer against five well-known machine learning models: Long Short-Term Memory network (LSTM), Bidirectional Long Short-Term Memory network (BiLSTM), Multi-layer Perceptron (MLP), Random Forest, and eXtreme Gradient Boosting model (XGBoost). For the deep learning models (LSTM, BiLSTM, MLP), the process of inputting remote sensing, climate data, and PFT data was

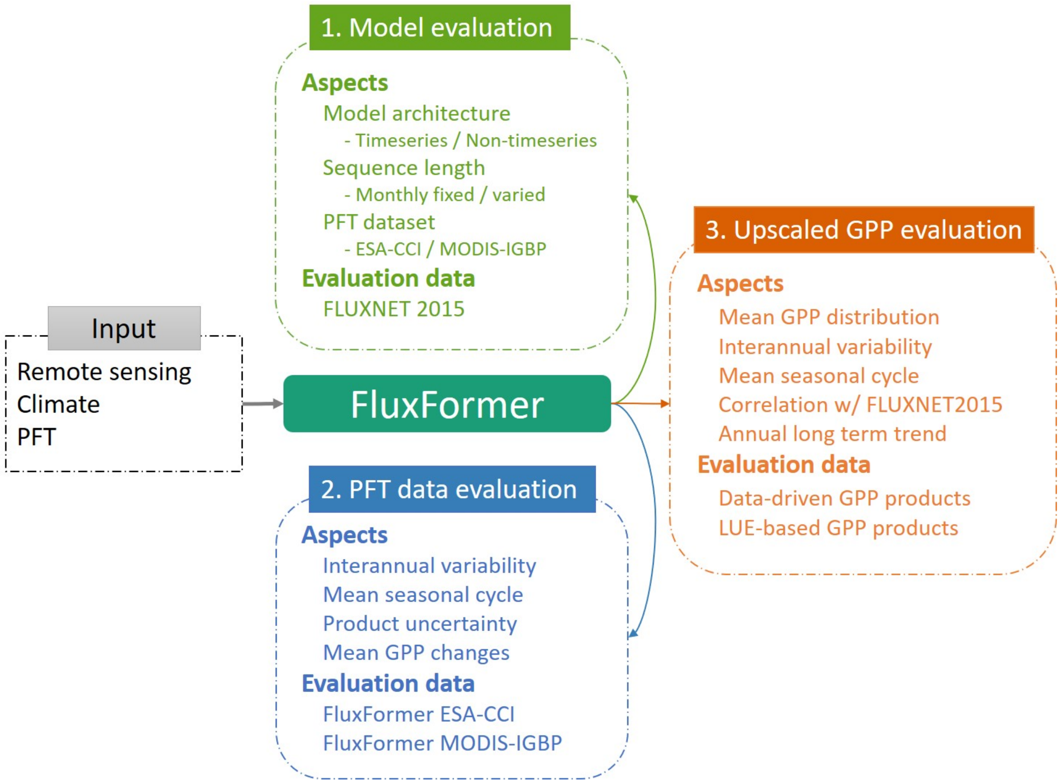

Figure 3. Validation framework for evaluating the proposed workflow in terms of model architecture, PFT dataset, and resulting GPP products.

consistent with that used in FluxFormer. This approach ensured that FluxFormer did not receive any special input treatment separate from the other models.

We assessed the performance of the model with and without the inclusion of PFT, as well as the performance of selected models using different PFT datasets (ESA-CCI, MODIS-IGBP, and their combination, ESA-CCI + MODIS-IGBP).

We aimed to identify the optimal time series length of input features for predicting monthly GPP. To do this, we initially trained a model using fixed sequence lengths of the input features, testing three scenarios: 1 month (1M), 6 months (6M), and 12 months (12M). For each scenario, we used the corresponding lag of input feature data: 1 month, 6 months, or 12 months prior to the monthly GPP observation time. Additionally, we varied the fixed time series lengths for GPP observed each month. Specifically, for a given month M, we used M months of lag data before the observed GPP month, starting from January. We referred to this case as "Jan to month M".

3.2.2 PFTs dataset evaluation

As discussed in the previous section, we assessed the effectiveness of two PFT datasets, ESA-CCI and MODIS-IGBP, in predicting monthly GPP with various machine learning models. This evaluation aims to determine the impact of each PFT dataset on global upscaled GPP products, utilizing the best-performing models identified in our model performance evaluation. To achieve this, we first examined the pixel-level interannual variability (IAV) of GPP from 2001 to 2020 by calculating the standard deviation divided by the mean of annual fluxes. Next we analyzed the seasonality of GPP by pixel-level correlation distribution with SIF due to its increasing use in GPP estimation (Norton et al., 2019; Liu et al., 2020; Bai et al., 2022). We select satellite SIF product from TROPOMI observation (Köhler et al., 2018) - TROPOSIF data for 2018 and 2019, as TROPOMI data is available only from 2018 onwards.

Additionally, we assessed the uncertainty introduced by each PFT dataset to its upscaled GPP product. For each PFT dataset, we trained five models separately through 150, 250, 350, 450, and 550 epochs. We then used the standard deviation of the annual mean and global annual mean variations of the five products from each PFT to evaluate the uncertainty introduced by the PFT to the GPP product. Finally, we investigated how differences in PFT distributions between the ESA-CCI and MODIS-IGBP datasets could affect the estimated GPP.

3.2.3 GPP products inter-comparison

We compare our upscaled GPP product with four other GPP products generated by data-driven models: FluxCom (Jung et al., 2019), NIES (Zeng et al., 2020), MetaFlux (Nathaniel et al., 2023), and Nirv-GPP (Wang et al., 2021). Additionally, we include two GPP products produced by light use efficiency models: LUE-SSVC (Bi et al., 2022), and LUE-VPM (Y. Zhang et al., 2017).

First, we examined the GPP annual mean distribution, latitudinal variations, and regional annual contributions of FluxFormer and other products. For regional contributions, we utilized the regional mask of the 26 SREX regions defined by the IPCC Special Report on Managing the Risks of Extreme Events and Disasters to Advance Climate Change Adaptation (Seneviratne et al., 2012). Figure A1 displays the masks for the 26 SREX regions.

Next, we analyzed GPP interannual variability (IAV) and seasonality using the same method employed in the previous section for evaluating upscaled GPP products derived from different PFT datasets. For the evaluation of GPP seasonality against SIF, some GPP products were not available after 2018 due to differences in data availability periods. Therefore, we focused our evaluation on the GPP seasonality of FluxCom, NIES, MetaFlux, and LUE-SSVC.

Then, we validated all GPP products against ground observations from the FLUXNET 2015 dataset. For data-driven models, re-evaluating these models with the same dataset used for training might seem inappropriate, as it could lead to overly optimistic results. This is because the same dataset is used for both training and validation. However, GPP products are typically generated at coarser spatial resolutions compared to the input data used for model training. For example, MODIS LAI (500m) and ESA CCI PFT (300m) data were used to extract feature values around the FLUXNET sites for model training, but the GPP product is produced at a 0.1-degree spatial resolution for computational efficiency. To produce a coarser-resolution GPP product, predictions must either be made on regridded/interpolated 0.1-degree input features or by regridding/interpolating high-resolution GPP predictions to a lower resolution (e.g., from 300m/500m to 0.1-degree). During this process, the trained model might still struggle to make accurate predictions from coarser input features or in neighboring pixels around the FLUXNET sites if high-resolution input features are used. This discrepancy can affect the final product through the regridding process from high-resolution to coarser resolution. Therefore, this evaluation is valuable for assessing discrepancies between GPP products, as demonstrated by Z. Zhang et al. (2024).

Finally, we examined the global interannual trends of the GPP product. To ensure consistent global area representation across all products, it is recommended by Jung et al. (2020) to compute the annual global mean GPP and RECO, scaling the global average fluxes using the total global land area of 122.4 million square kilometers (M. A. Friedl et al., 2010). However, we observed that each GPP product has its own no-data mask for desert or polar areas. Therefore, we decided to preserve the masking purpose of the data provided and calculate the global annual GPP by summing its latitude-weighted pixels rather than scaling global mean GPP by global land area.

4 Results

4.1 Model performance evaluation

First, we presented the cross-validation scores for six models: FluxFormer, LSTM, BiLSTM, MLP, RF, and XGB, across four PFT dataset settings: Without PFT, ESA-CCI, MODIS-IGBP, and MODIS-IGBP + ESA-CCI, and four timeseries settings: one case of varied sequence length (Jan to month M), and three cases of fixed sequence length (1M, 6M, and 12M), as detailed in Table S1 and Figure 4.

Overall, FluxFormer achieved the highest performance with varied sequence lengths (Jan to month M) and with PFT incoporated. The models were able to explain approximately 73% of the variation in monthly GPP through cross-validation.

Incorporating PFT generally improved the performance of all models and reduced the error across different timeseries settings. In the case of varied timeseries lengths (Jan to month M), models with PFT significantly outperformed those without PFT, explaining approximately 2% to 5% more variation in monthly GPP. For fixed time series lengths (1M, 6M, and 12M), PFT-included models such as FluxFormer, Random Forest, and XGBoost achieved R^2 values that were 3% to 6% higher compared to models without PFT. However, for LSTM, BiLSTM, and MLP, the improvement was around 1%. Including PFT is crucial as it provides contextual information that enhances the learning process for all models in predicting monthly GPP on a global scale.

Despite differences in content between ESA-CCI, which provides 2D data on local PFT fractions, and MODIS-IGBP, which offers 1D data on the most dominant PFT while ignoring others, the performance improvement from these two PFT datasets is largely similar in terms of predicting monthly GPP, as evaluated using R^2 and RMSE scores across global-scale cross-validation. Additionally, the definitions of PFTs differ significantly between ESA-CCI (14 classes) and MODIS-IGBP (17 classes). Therefore, it is necessary to evaluate the models in local regions and further assess the GPP products generated by each PFT dataset, as discussed later in this study.

For fixed sequence length settings, all models performed poorly with a 1-month lag of the input feature (1M case), and their performance improved as the sequence length increased from 1M to 6M. However, extending the length to 12M (12 months), which involves inputting a sequence of at least 44 8-day records of remote sensing and climate data, generally did not enhance the models' performance compared to the 6M case. This is likely due to the noise from redundant information in the 12M case degrading the models' performance. For varied sequence lengths, FluxFormer, BiLSTM, and MLP achieved better results than with fixed lengths, with FluxFormer delivering the best overall performance, showing the R^2 and lowest RMSE, as shown in Figure 4 (a) to (c). Using inputs with monthly varied sequence lengths not only achieves comparable performance, and even better results for FluxFormer, but is also more efficient in terms of model complexity compared to using long fixed sequences (6M and 12M). This approach requires 12 monthly models but uses significantly less training data per model compared to training a single model with fixed sequence lengths using the entire dataset.

Incorporating varied sequence lengths into FluxFormer has yielded the best overall performance. To avoid redundancy and distractions from plotting fixed sequence length models, Figures 5 and 6 focus on the performance of the six models using only varied sequence lengths of input data with four PFT settings. These figures are evaluated against

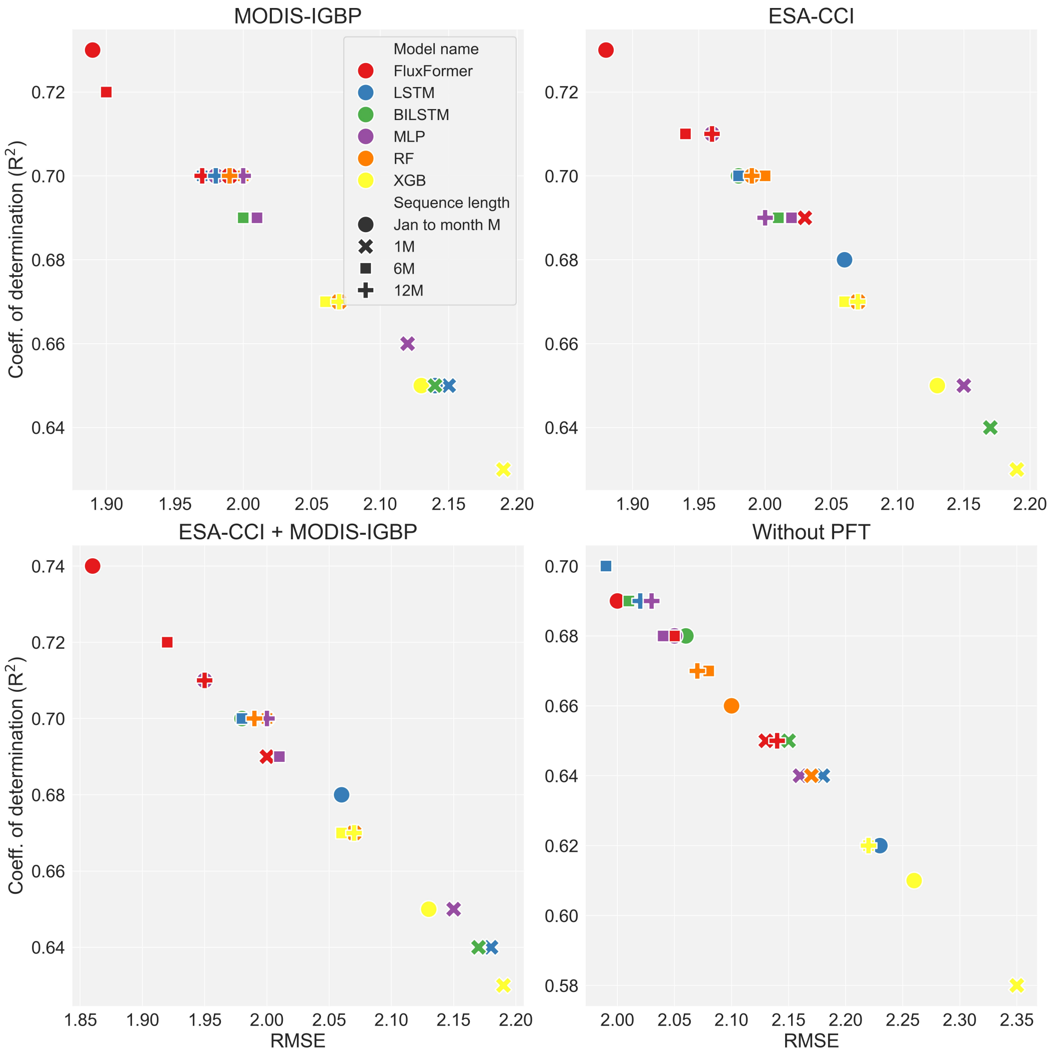

Figure 4. Performance of FluxFormer, LSTM, BiLSTM, MLP, Random Forest, and XGBoost in predicting monthly GPP across global scale, with varying monthly sequence lengths and different PFT data settings.

monthly observed GPP and the mean seasonal cycle across five climate regions: tropical, arid, temperate, continental, and polar. In terms of monthly GPP, FluxFormer with different PFT settings consistently shows the highest performance in the tropical, temperate, continental, and polar regions. However, in the arid region, BiLSTM achieves the highest performance among the models. The ESA-CCI dataset significantly outperforms MODIS-IGBP in both the tropical region (with FluxFormer) and the arid region (with BiLSTM).

In terms of the mean seasonal cycle, FluxFormer shows the highest performance in the tropical, temperate, and continental regions, with $R^2 > 0.95$. In the arid region, FluxFormer significantly outperforms the other models, with R^2 ranging from 0.14 to 0.61, while the other models have $R^2 < 0$. In the polar region, FluxFormer achieves the second-best $R^2 = 0.91$, following LSTM with $R^2 = 0.92$, both models use the combination of MODIS-IGBP and ESA-CCI. Detailed performance metrics for all models are provided in Table S2 and S3.

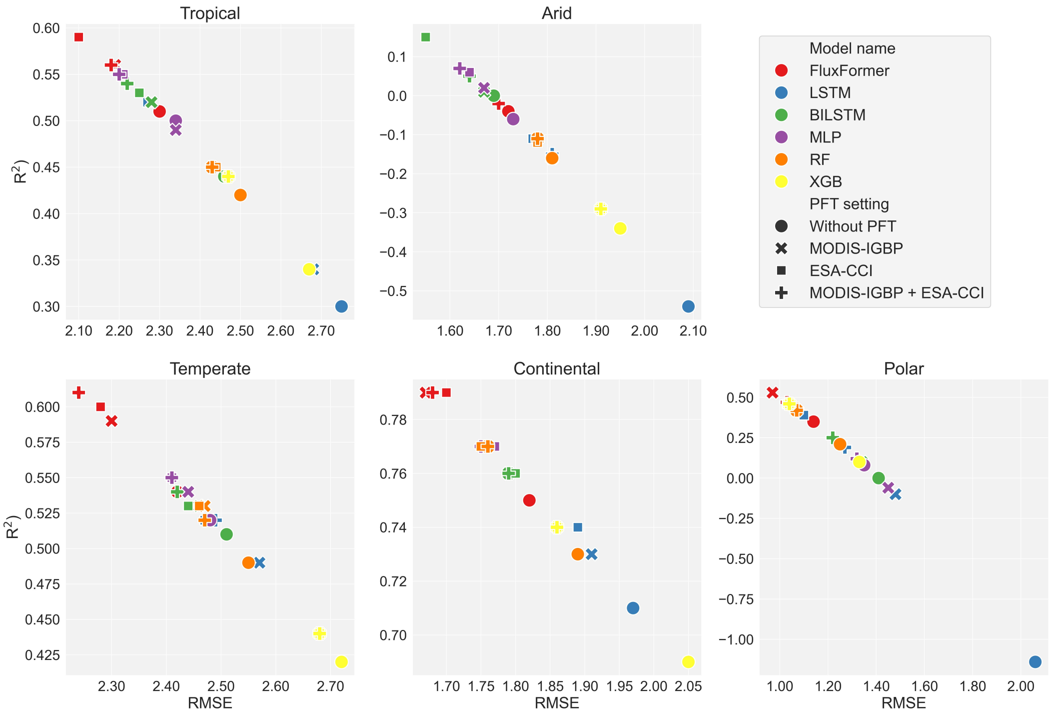

Figure 5. Performance of FluxFormer, LSTM, BiLSTM, MLP, Random Forest, and XGBoost in predicting monthly GPP across various local climate regions, with varying monthly sequence lengths and different PFT data settings.

In general, cross-validation of various deep learning model architectures including MVTS, LSTM, BiLSTM, MLP, and traditional machine learning models such as Random Forest and XGBoost, along with different PFT settings and input sequence lengths, showed that FluxFormer achieved the best performance. This model, based on the MVTS architecture and utilizing varied sequence lengths (from January to month M) and PFT, demonstrated the highest effectiveness. However, this evaluation did not clarify the impact of MODIS-IGBP, ESA-CCI, or their combination. Therefore, a detailed assessment in the next section will evaluate how these two PFT datasets affect the generated GPP products.

4.2 PFTs Dataset evaluation

We show the GPP IAV of FluxFormer with four PFT settings in Figure 7. We observed that the GPP product from ESA-CCI exhibits the lowest variability in desert regions such as Australia, West and Central Asia, Southern Africa, and parts of North America. This aligns with the expected low GPP in these areas (Hadley & Szarek, 1981), suggesting greater plausibility for the ESA-CCI PFT dataset in these regions. While MODIS-IGBP derived GPP product can reduce IAV in some arid regions compared to the product without using PFT, its IAV in Australia and the Arabian Peninsula is clearly higher. The combination of the two PFT datasets also reduces IAV in some arid regions compared to the other settings, but it still has higher IAV in Australia than ESA-CCI, likely due to the influence of MODIS-IGBP data. For the mean seasonal cycle evaluation shown in Figure 8, all the products exhibit a similar pattern in Pearson correlation with TROPOSIF in 2018 and 2019. The highest correlations are observed in temperate and continental regions, while the lowest correlations are found in tropical and arid regions. The clear-

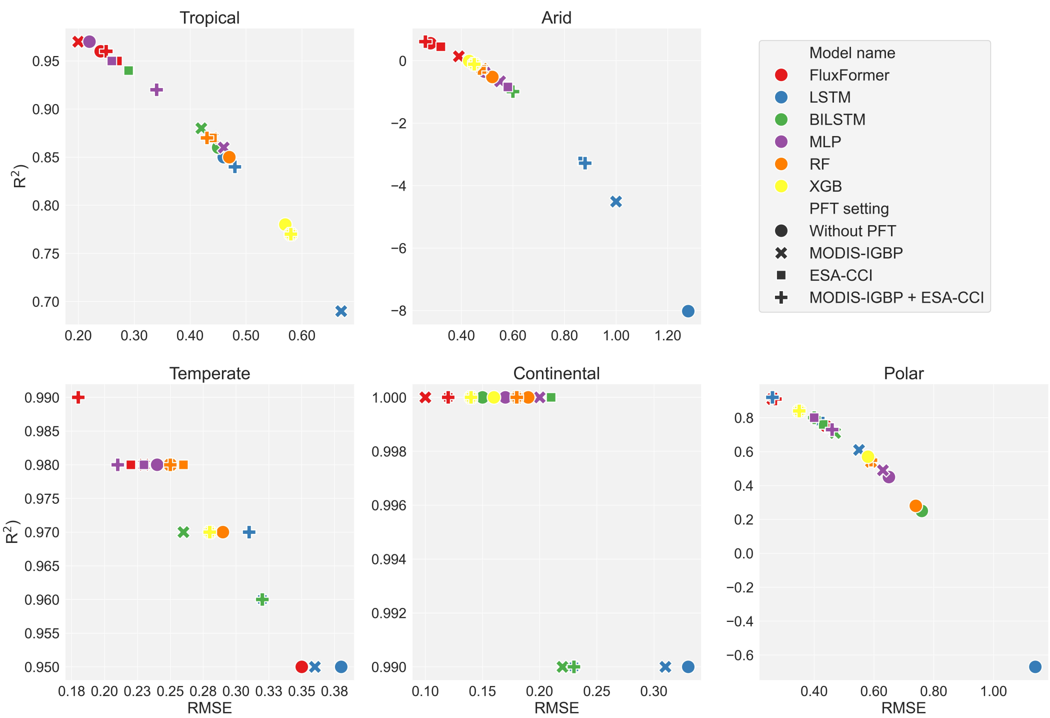

Figure 6. Performance of FluxFormer, LSTM, BiLSTM, MLP, Random Forest, and XG-Boost in predicting monthly GPP mean seasonal cycle various local climate regions, with varying monthly sequence lengths and different PFT data settings.

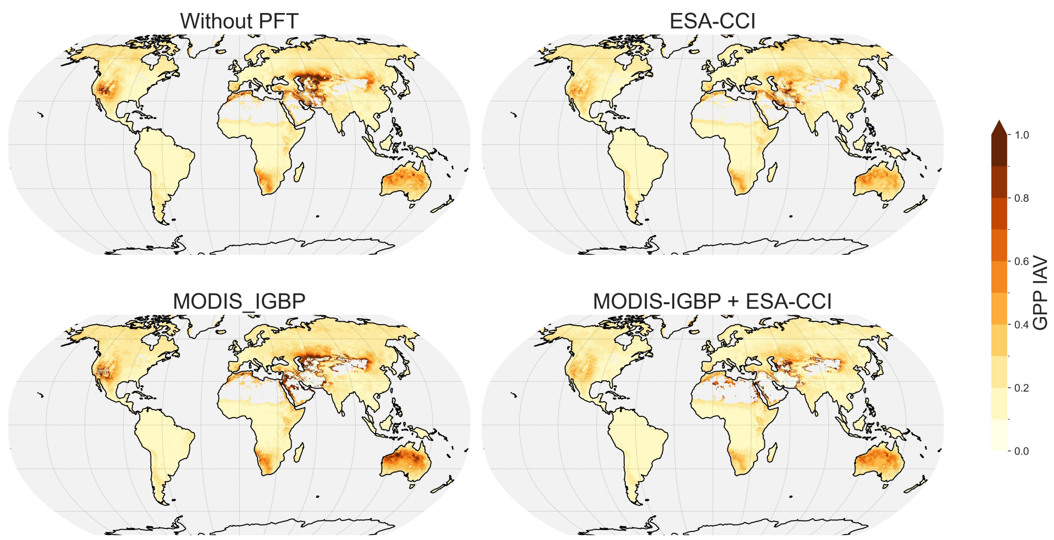

Figure 7. Spatial patterns of GPP interannual variability extracted over 2001 to 2021 for FluxFormer with different setting of PFT data.

est difference between the products is seen in the Northeast Brazilian forest, with minor differences observed in East Africa.

Figure 9(a) shows the pixel-level uncertainty of the generated products from the trained model with different epochs and PFT settings for the year 2001, while Figure

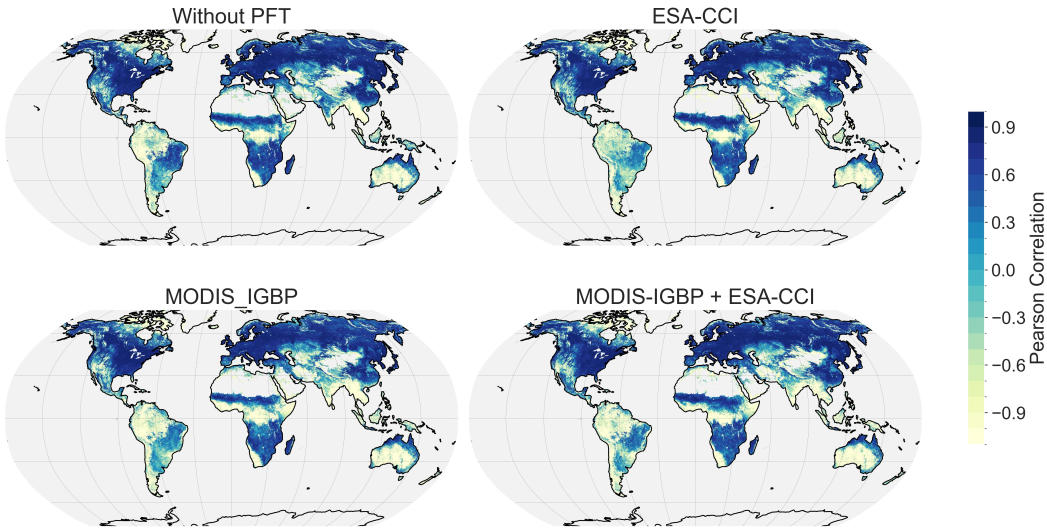

Figure 8. Spatial patterns of mean seasonal correlation with TROPOSIF over 2018 to 2019 for FluxFormer with different setting of PFT data.

9(b) presents the global interannual trend from 2001 to 2020. The lowest uncertainty is observed with the ESA-CCI dataset, while the highest is seen with the MODIS-IGBP dataset in both spatial (pixel-level) and temporal (long-term trend) aspects. In fact, using MODIS-IGBP results in greater uncertainty than not using any PFT data at all. The MODIS-IGBP-derived product shows the highest uncertainties, particularly in regions like the southern Sahara and eastern North America. Conversely, the lowest uncertainties are found in tropical regions, consistently covered by evergreen broadleaf forests. Since these products were generated using models trained with varying numbers of epochs, ranging from 150 to 550, we found that the MODIS-IGBP data could easily introduce noise to the model, leading to instability after each training session, especially with varying epoch numbers. Using ESA-CCI reduces the product's uncertainty across models, suggesting that products generated with ESA-CCI are more reliable than those using the MODIS-IGBP PFT dataset or no PFT dataset at all.

In addition to the earlier uncertainty analysis, we evaluate how differences in PFT distributions between the ESA-CCI and MODIS-IGBP datasets could impact the estimated GPP, as shown in Figure 10. ESA-CCI and MODIS-IGBP define PFT classes differently: ESA-CCI uses 14 classes in a 2D format, while MODIS-IGBP uses 17 classes in a 1D format. To facilitate comparison, we regrouped the PFT classes into three main categories: Tree, Shrub, and Grass.

For ESA-CCI, the Tree class includes of four subclasses: broadleaved deciduous (BD) trees, broad-leaved evergreen (BE) trees, needle-leaved deciduous (ND) trees, and needle-leaved evergreen (NE) trees. The Shrub class also has four subclasses: BD shrubs, BE shrubs, ND shrubs, and NE shrubs, while the Grass class encompasses both natural and managed grasses. For MODIS-IGBP, the Tree class consists of five subclasses: BD forests, BE forests, ND forests, NE forests, and mixed forests. We specifically select only closed shrublands for the Shrub category, while the Grass class was grouped from open shrublands, woody savannahs, savannahs, grasslands, and croplands.

This regrouping highlights differences in PFT coverage and accounts for variations in GPP between the two datasets. As shown in Figure 10(a), the mean annual GPP for 2001 differs between ESA-CCI and MODIS-IGBP. Figure 10(b) depicts differences in the

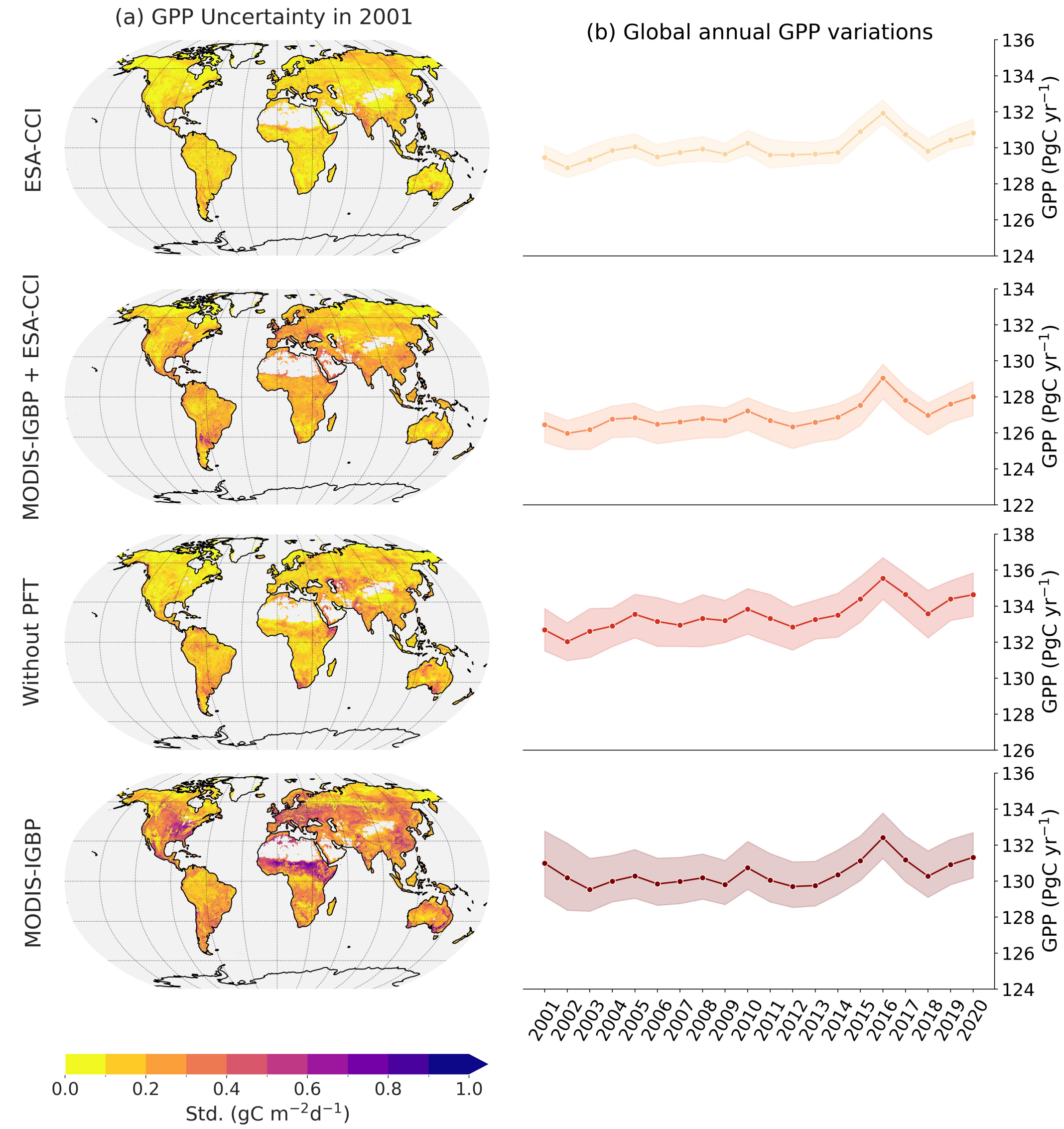

Figure 9. (a) Spatial patterns of uncertainty of FluxFormer with differnt setting of PFT data in 2001 and (b) global interannual variability for FluxFormer with different setting of PFT data over 2001 to 2021.

three main PFT categories. MODIS-IGBP's 1D data underrepresents tree cover in northern Asia, North America, Central Africa, East Asia, and parts of South America, leading to lower GPP estimates compared to ESA-CCI. In Central Europe, ESA-CCI shows slightly lower tree coverage than MODIS-IGBP, resulting in lower GPP estimates. In tropical regions dominated by broad-leaved evergreen tree, no significant difference in tree cover as well as GPP estimates is observed between the two PFT datasets.

For Shrub categories, even though open shrublands and woody savannahs are included in Grass in MODIS-IGBP, the differences in Shrub coverage between MODIS-IGBP and ESA-CCI are relatively minor compared to those for Tree and Grass, highlighting discrepancies in Shrub definitions in each dataset. Lastly, ESA-CCI shows lower grass coverage than MODIS-IGBP, particularly in northern Asia, North America, southeastern South America, South Africa, and Australia, resulting in slightly lower GPP estimates. This experiment demonstrates how variations in PFT distributions and definitions across different datasets can impact GPP estimates.

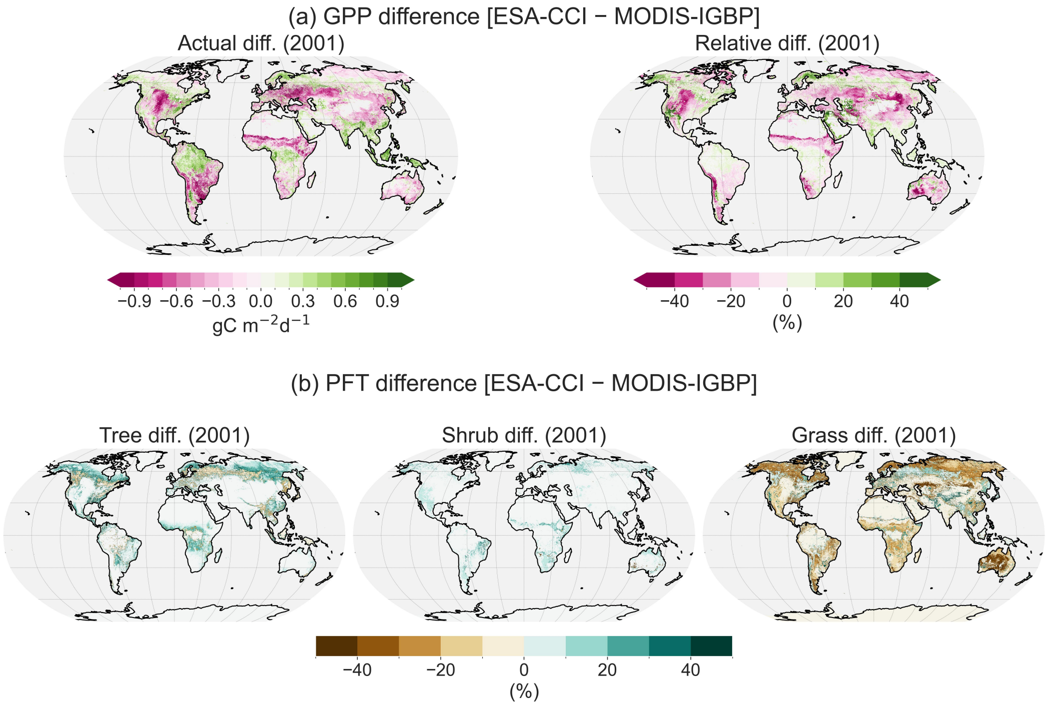

Figure 10. The difference in derived GPP product (a) and PFT cover (b) between ESA-CCI and MODIS-IGBP.

After evaluating GPP IAV, mean seasonal cycles, and the uncertainty of the generated GPP products and the GPP changes induced by different PFT datasets, we found that ESA-CCI outperforms the MODIS-IGBP dataset in terms of spatial IAV and overall product reliability. The mean seasonal cycle is primarily influenced by the choice of model architecture and sequence length. Therefore, in the final comparison with other GPP products, we will exclusively use the ESA-CCI-derived GPP product.

4.3 GPP products inter-comparison

Figure 11 illustrates the average GPP and RECO values for all products in 2016. As expected, GPP is highest in tropical regions and lowest in semi-arid areas. As shown in Figure 12(a), a consistent pattern of the latitudinal distribution of GPP emerges across all products, with GPP values gradually increasing from colder climates to warm and humid conditions in temperate and tropical regions.

Notably, the largest differences between product estimates occur in tropical regions (particularly in the Amazon, West Africa, Southeast Asia) and North Asia of FluxCom and MetaFlux compared to the others, as indicated in Figure 12(b). These differences are likely due to two main factors. First, the lack of reliable observations in tropical regions and North Asia, which are major contributors to GPP, is due to the sparse distribution of FluxNet sites. In contrast, Europe and North America have a denser network of observation sites but contribute less to overall GPP. Second, variations in input data and methodological approaches across different studies also contribute to these discrepancies.

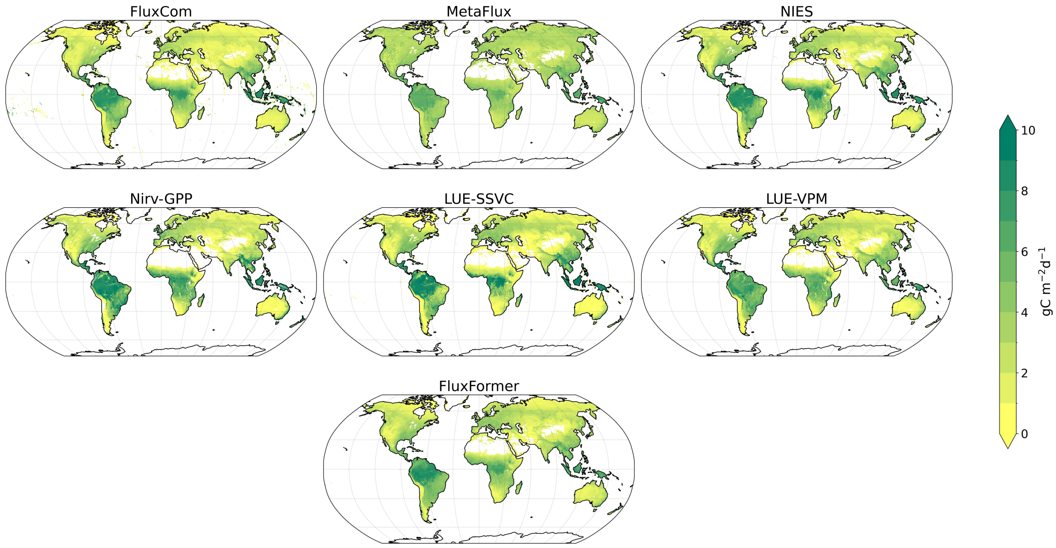

Figure 11. Global distribution of mean annual GPP in 2016 from FluxFormer and other upscaled products.

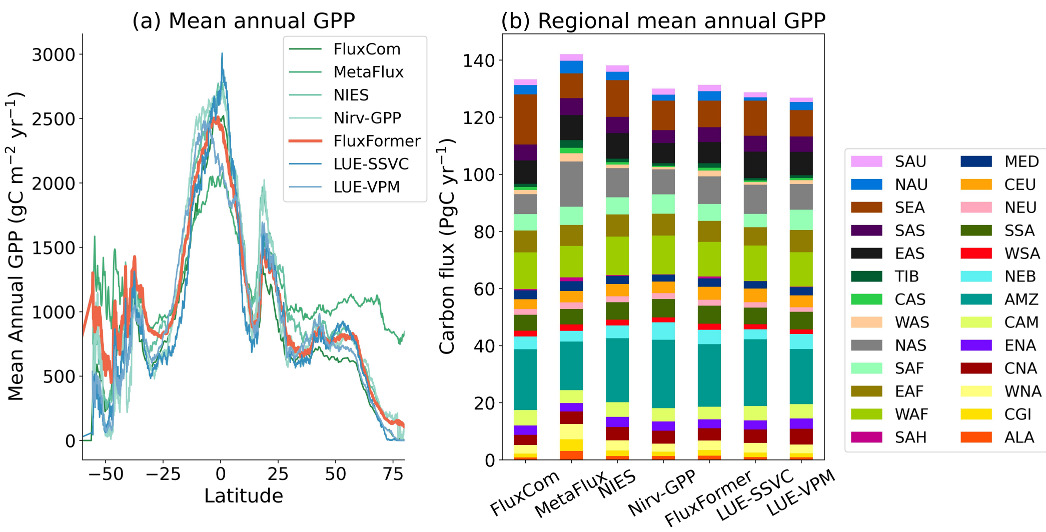

Figure 12. (a) Latitudinal distributions of mean annual and (b) regional GPP from SREX regions from FluxFormer and other upscaled product over 2001 to 2020

Focusing on interannual variations (Figure 13), we find that our GPP data exhibits lower variability compared to Nirv-GPP, LUE-VPM in desert regions like parts of Australia, Eastern and Southern Africa, and parts of North and South America. This aligns with the expected low GPP in these areas (Hadley & Szarek, 1981), suggesting greater plausibility of our data in these regions. FluxCom, LUE-SSVC, and MetaFlux show the least variability among the datasets. However, their interannual variability may be underestimated relative to other approaches, such as inversion models and DGVMs (Jung et al., 2020).

While a linear relationship between GPP and SIF has been widely assumed in previous studies (Guanter et al., 2012; H. Yang et al., 2017), this assumption remains un-

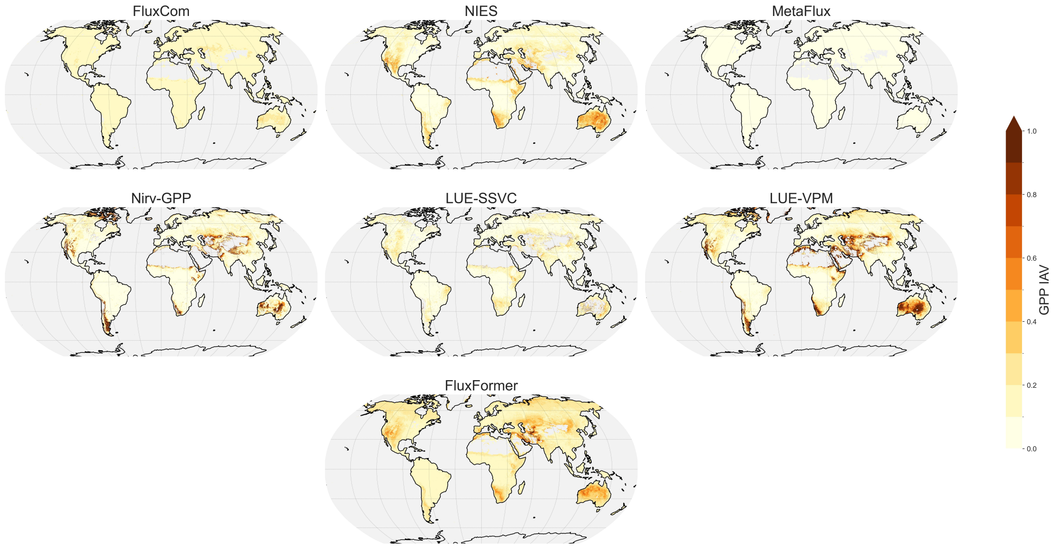

Figure 13. Spatial patterns of GPP interannual variability extracted over 2001 to 2021 from FluxFormer and other upscaled products.

certain across diverse climate regions and PFTs (Gu et al., 2019; Xiao et al., 2019; Y. Zhang et al., 2016; A. Chen et al., 2021). This uncertainty is particularly pronounced in tropical regions, where weak seasonality in photosynthesis leads to a less robust linear relationship between SIF and GPP (Doughty et al., 2021). Regionally, tropical forests and savannahs are often water-limited rather than sunlight-limited (Guan et al., 2015; Madani et al., 2017, 2020; Palmer et al., 2023). Furthermore, tropical forests, dominated by evergreen broadleaf forests (EBFs), exhibit complex vegetation structures that contribute to larger uncertainties in both satellite observations and ground-based GPP estimates from EC sites, further weakening the SIF-GPP correlation in these regions (Hayek et al., 2018; Li et al., 2018; Z. Zhang et al., 2020; Shekhar et al., 2022). Additionally, frequent cloud cover in the tropics contaminates SIF signals from satellite observations, adding to the challenge of using SIF as a reliable proxy for GPP (Doughty et al., 2021; Shekhar et al., 2022).

Figure 14 depicts the temporal correlations between monthly SIF and GPP. In temperate and continental regions, most products show moderate to high GPP-SIF correlations. However, in arid regions, FluxFormer show lower GPP-SIF correlations, especially in the Horn of Africa deserts. This corresponds with the findings of Palmer et al. (2023), highlighting the more substantial influence of rainfall on GPP than sunlight in this eastern desert region of Africa. In tropical regions, our data shows lower correlations with TROPOMI SIF compared to FluxCom, NIES, and MetaFlux, particularly in Central/South America, West/Central Africa, and Southeast Asia. This aligns with observations from previous studies (Sanders et al., 2016; Doughty et al., 2021; Shekhar et al., 2022), suggesting weak seasonality in tropical photosynthesis weakens the GPP-SIF correlation to background levels.

In addition to evaluating the GPP product with SIF, we re-assessed the GPP products using the FLUXNET 2015 dataset. This re-evaluation included both monthly GPP and the mean seasonal cycle to further examine differences in GPP seasonality in tropical regions, which showed low seasonal consistency among the products after the TROPOSIF evaluation. As noted earlier, this re-evaluation is important because the GPP product has a coarser resolution compared to the original input used for model training. The results, shown in Figure 15 present the R^2 values across five climate regions for all mod-

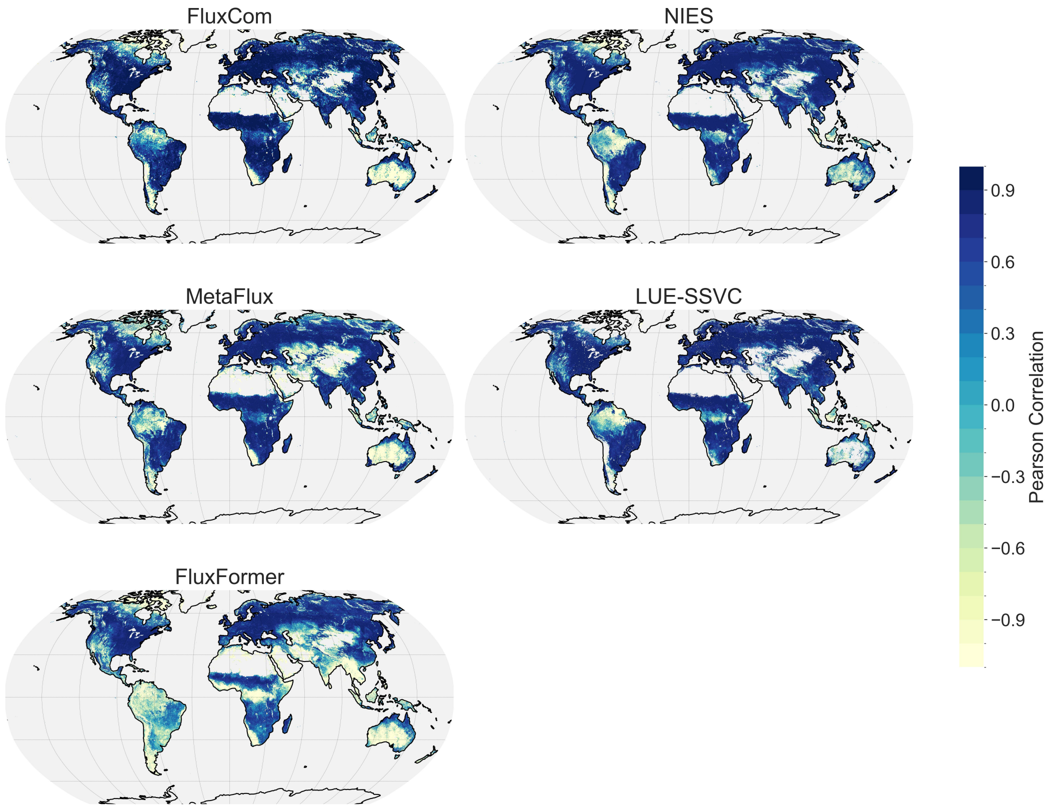

Figure 14. Spatial patterns of mean seasonal correlation with TROPOSIF over 2018 to 2019 from FluxFormer and other upscaled products.

els. FluxFormer demonstrates the highest R^2 values for monthly observed GPP and the mean seasonal cycle, particularly in tropical regions and most other regions, except the arid region, where FluxFormer achieves a second-best $R^2 = 0.85$, following NIES $R^2 = 0.87$. This indicates that FluxFormer shows much better agreement with ground-observed GPP than other products at both regional and global scales, in terms of monthly observed GPP and seasonal trends. However, due to the complexity of tropical rainforests, and sparse EC sites impede accurate quantification of seasonal carbon fluxes (Xu et al., 2015), including their reliance on groundwater for photosynthesis and the lack of groundwater data (Z. Zhang et al., 2024), it is essential to further re-assess GPP seasonality in tropical regions in future studies.

Examining the global annual mean time series of GPP from 2001 to 2020, as shown in Figure 16(a), reveals diverse patterns in carbon fluxes across different products. Estimated annual mean fluxes for GPP range from 120 to 145 PgC/year, with FluxFormer and other products falling within this range. Among these, LUE model-derived products (LUE-SSVC and LUE-VPM) show a more pronounced positive GPP trend compared to data-driven products (FluxCom, MetaFlux, NIES, Nirv-GPP, and FluxFormer), as illustrated in Figure 16(b). Among the data-driven products, the GPP trend from FluxCom is considered unrealistic as it does not account for the CO_2 fertilization effect (Jung et al., 2020). Other data-driven products show positive trends, with MetaFlux having the smallest trend at 0.03 PgC/year, NIES showing the largest trend at 0.38 PgC/year, followed by Nirv-GPP at 0.30 PgC/year, and FluxFormer at 0.21 PgC/year. These positive GPP trends align with the anticipated increase due to the CO_2 fertilization effect,

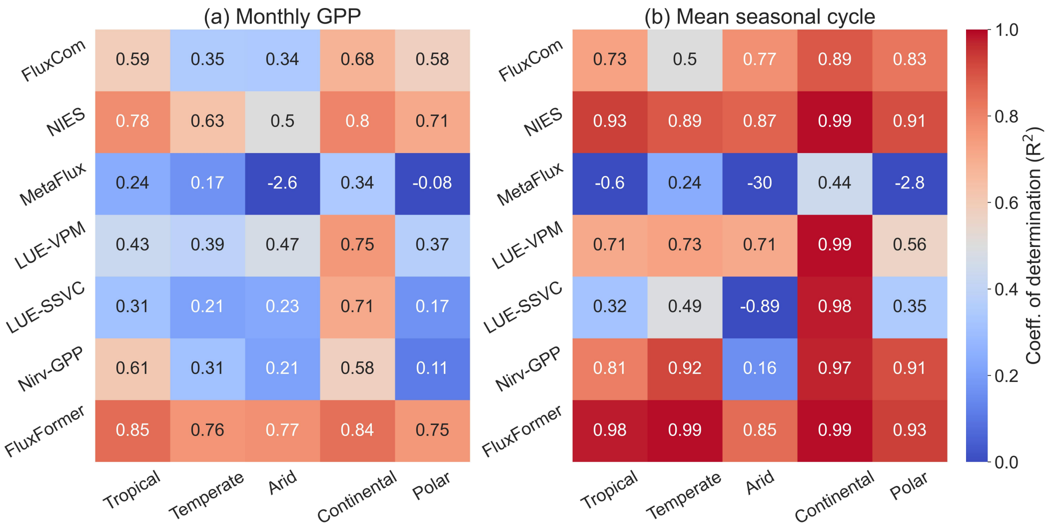

Figure 15. The coefficient of determination R^2 of FluxFormer and other upscaled products against FLUXNET 2015 dataset (a) for monthly GPP and (b) for mean seasonal cycle.

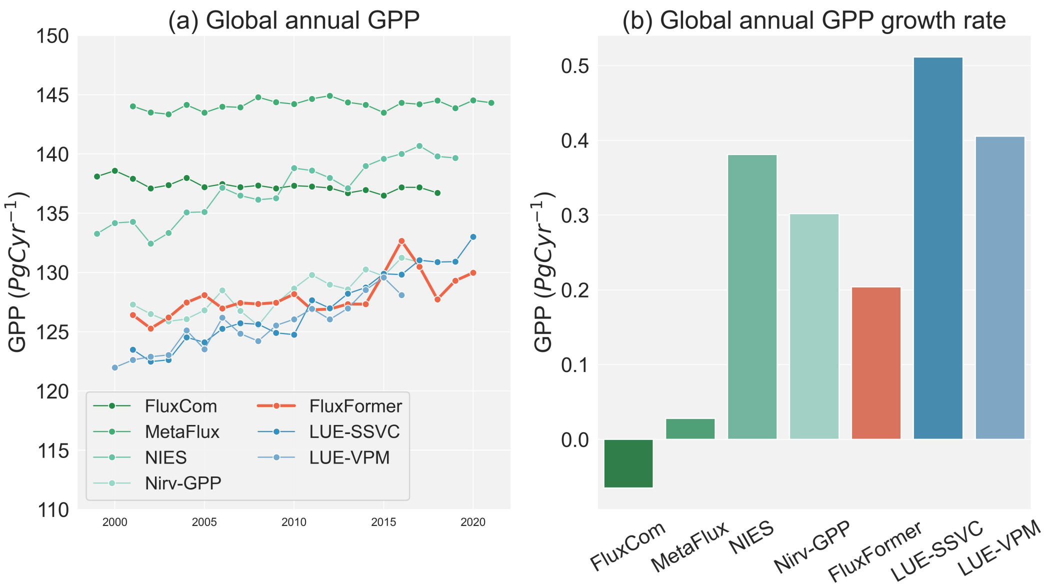

Figure 16. Global annual GPP variations (a) and GPP grow rate (b) from FluxFormer and other upscaled products over 2001 to 2020.

which could potentially enhance the land carbon sink (Piao et al., 2020; R. Yang et al., 2022; Guo et al., 2023).

5 Conclusion

In this study, we present our work on upscaling global gross primary production. We first evaluated different aspects of the upscaling framework, including the choice of time series model architecture, optimal sequence length for input data, and the selection of an appropriate PFT dataset through cross-validation. We then compared the GPP dataset generated using the best model configuration, including architecture, sequence length, and PFT settings, with other satellite-based upscaled products.

Our cross-validation against FLUXNET 2015 data revealed that FluxFormer outperformed models such as LSTM, BiLSTM, MLP, Random Forest, and XGBoost in monthly GPP predicting skill. FluxFormer, utilizing either the ESA-CCI or MODIS-IGBP PFT datasets, achieved a R^2 of 73%, surpassing other models with similar input data and training pipelines. It demonstrated promising performance, particularly in predicting GPP in tropical regions.

The comparison of GPP products using ESA-CCI and MODIS-IGBP datasets revealed that the MVTS Transformer model, combined with an optimal input data sequence length, significantly improves monthly GPP predictions and the mean seasonal cycle, while also reducing model complexity and computational burden. The choice of PFT dataset has a substantial impact on GPP estimates, interannual variability, and overall product uncertainty. Specifically, the ESA-CCI dataset offers more reliable GPP data compared to MODIS-IGBP and is recommended for future GPP upscaling studies.

Inter-comparison with other upscaled GPP products (FluxCom, NIES, MetaFlux, Nirv-GPP, LUE-SSVC, LUE-VPM) shows that FluxFormer aligns well with latitudinal variations and spatial distribution of mean annual GPP. However, notable discrepancies are observed in tropical regions and North Asia, particularly with FluxCom and MetaFlux. FluxFormer exhibits lower interannual variability in arid regions compared to Nirv-GPP and LUE-VPM, consistent with expected low GPP in these areas (Hadley & Szarek, 1981). The mean seasonal cycle analysis using TROPOMI SIF indicates strong GPP-SIF correlations in cold and temperate regions but lower correlations in tropical and semi-arid regions, reflecting weaker seasonality in tropical photosynthesis (Sanders et al., 2016; Doughty et al., 2021; Shekhar et al., 2022). From 2001 to 2020, FluxFormer shows a positive GPP trend with a growth rate of 0.21 PgC per year, aligning with other products and supporting the CO_2 fertilization effect (Piao et al., 2020; R. Yang et al., 2022; Guo et al., 2023).

Overall, our study shows that using the MVTS Transformer encoder with varying sequence lengths each month improves monthly GPP predictions and the mean seasonal cycle. Additionally, the ESA-CCI PFT dataset provides more reliable GPP estimates than the MODIS-IGBP dataset.

Open Research Section

The data for this study is publicly available as follows: FLUXNET 2015 (Pastorello et al., 2020), LAI and FPAR from MOD15A2H.061 8-day data (`https://developers.google.com/earth-engine/datasets/catalog/MODIS_061_MOD15A2H`), climate data from ERA5 reanalysis (Muñoz Sabater, 2019), global PFT dataset v2.0.8 (Harper et al., 2022), TROPOMI SIF (Köhler et al., 2018) (`ftp://fluo.gps.caltech.edu/data/tropomi/`), FluxFormer (Phan & Fukui, 2023), NIES dataset (Zeng et al., 2020), FluxCom dataset (Jung et al., 2019), MetaFlux dataset (Nathaniel et al., 2023), Nirv-GPP dataset (Wang et al., 2021), LUE-SSVC dataset (Bi et al., 2022), LUE-VPM dataset (Y. Zhang et al., 2017). The source code for MVTS Transformer (Zerveas et al., 2021) can be found at the Gihub repository (`https://github.com/gzerveas/mvts_transformer`).

Acknowledgments

This work was supported by the Ministry of Education, Culture, Sports, Science and Technology - Japan, and the International Digital Earth Applied Science Research Center at Chubu University.

References

Bai, J., Zhang, H., Sun, R., Li, X., Xiao, J., & Wang, Y. (2022). Estimation of global gpp from gome-2 and oco-2 sif by considering the dynamic variations of gpp-sif relationship. *Agricultural and Forest Meteorology*, *326*, 109180.

Beer, C., Reichstein, M., Tomelleri, E., Ciais, P., Jung, M., Carvalhais, N., ... others (2010). Terrestrial gross carbon dioxide uptake: global distribution and covariation with climate. *Science*, *329*(5993), 834–838.

Besnard, S., Carvalhais, N., Arain, M. A., Black, A., Brede, B., Buchmann, N., ... Reichstein, M. (2019, 02). Memory effects of climate and vegetation affecting net ecosystem co2 fluxes in global forests. *PLOS ONE*, *14*(2), 1-22. Retrieved from `https://doi.org/10.1371/journal.pone.0211510` doi: 10.1371/journal.pone.0211510

Bi, W., He, W., Zhou, Y., Ju, W., Liu, Y., Liu, Y., ... Cheng, N. (2022, May 16). A global 0.05° dataset for gross primary production of sunlit and shaded vegetation canopies from 1992 to 2020. *Scientific Data*, *9*(1), 213. Retrieved from `https://doi.org/10.1038/s41597-022-01309-2` doi: 10.1038/s41597-022-01309-2

Burba, G. G., McDermitt, D. K., Grelle, A., Anderson, D. J., & Xu, L. (2008). Addressing the influence of instrument surface heat exchange on the measurements of co2 flux from open-path gas analyzers. *Global Change Biology*, *14*(8), 1854-1876. Retrieved from `https://onlinelibrary.wiley.com/doi/abs/10.1111/j.1365-2486.2008.01606.x` doi: https://doi.org/10.1111/j.1365-2486.2008.01606.x

Chen, A., Mao, J., Ricciuto, D., Lu, D., Xiao, J., Li, X., ... Knapp, A. K. (2021). Seasonal changes in gpp/sif ratios and their climatic determinants across the northern hemisphere. *Global Change Biology*, *27*(20), 5186–5197.

Chen, M., Rafique, R., Asrar, G. R., Bond-Lamberty, B., Ciais, P., Zhao, F., ... others (2017). Regional contribution to variability and trends of global gross primary productivity. *Environmental Research Letters*, *12*(10), 105005.

Cranko Page, J., Abramowitz, G., De Kauwe, M. G., & Pitman, A. J. (2024). Are plant functional types fit for purpose? *Geophysical Research Letters*, *51*(1), e2023GL104962. Retrieved from `https://agupubs.onlinelibrary.wiley.com/doi/abs/10.1029/2023GL104962` (e2023GL104962 2023GL104962) doi: https://doi.org/10.1029/2023GL104962

Díaz, E., Adsuara, J. E., Martínez, Á. M., Piles, M., & Camps-Valls, G. (2022, Jan 31). Inferring causal relations from observational long-term carbon and water fluxes records. *Scientific Reports*, *12*(1), 1610. Retrieved from `https://doi.org/10.1038/s41598-022-05377-7` doi: 10.1038/s41598-022-05377-7

Doughty, R., Xiao, X., Köhler, P., Frankenberg, C., Qin, Y., Wu, X., ... Moore III, B. (2021). Global-scale consistency of spaceborne vegetation indices, chlorophyll fluorescence, and photosynthesis. *Journal of Geophysical Research: Biogeosciences*, *126*(6), e2020JG006136.

FLUXNET. (2024). *Fluxnet site list.* (`https://fluxnet.org/sites/site-list-and-pages/` [Accessed: (2024/08/04)])

Friedl, M., & Sulla-Menashe, D. (2019). *MCD12Q1 MODIS/Terra+Aqua land cover type yearly L3 global 500m SIN grid V006.* NASA EOSDIS Land Processes Distributed Active Archive Center.

Friedl, M. A., Sulla-Menashe, D., Tan, B., Schneider, A., Ramankutty, N., Sibley, A., & Huang, X. (2010). Modis collection 5 global land cover: Algorithm refinements and characterization of new datasets. *Remote sensing of Environment*, *114*(1), 168–182.

Friedlingstein, P., O'Sullivan, M., Jones, M. W., Andrew, R. M., Bakker, D. C. E., Hauck, J., ... Zheng, B. (2023). Global carbon budget 2023. *Earth System Science Data*, *15*(12), 5301–5369. Retrieved from `https://essd.copernicus.org/articles/15/5301/2023/` doi: 10.5194/essd-15-5301-2023

Gaber, M., Kang, Y., Schurgers, G., & Keenan, T. (2024). Using automated machine learning for the upscaling of gross primary productivity. *Biogeosciences*, *21*(10), 2447–2472. Retrieved from https://bg.copernicus.org/articles/21/2447/2024/ doi: 10.5194/bg-21-2447-2024

Gorelick, N., Hancher, M., Dixon, M., Ilyushchenko, S., Thau, D., & Moore, R. (2017). Google earth engine: Planetary-scale geospatial analysis for everyone. *Remote Sensing of Environment*, *202*, 18-27. Retrieved from https://www.sciencedirect.com/science/article/pii/S0034425717302900 (Big Remotely Sensed Data: tools, applications and experiences) doi: https://doi.org/10.1016/j.rse.2017.06.031

Gu, L., Han, J., Wood, J. D., Chang, C. Y.-Y., & Sun, Y. (2019). Sun-induced chl fluorescence and its importance for biophysical modeling of photosynthesis based on light reactions. *New Phytologist*, *223*(3), 1179–1191.

Guan, K., Pan, M., Li, H., Wolf, A., Wu, J., Medvigy, D., ... others (2015). Photosynthetic seasonality of global tropical forests constrained by hydroclimate. *Nature Geoscience*, *8*(4), 284–289.

Guanter, L., Frankenberg, C., Dudhia, A., Lewis, P. E., Gómez-Dans, J., Kuze, A., ... Grainger, R. G. (2012). Retrieval and global assessment of terrestrial chlorophyll fluorescence from gosat space measurements. *Remote Sensing of Environment*, *121*, 236–251.

Guo, R., Chen, T., Chen, X., Yuan, W., Liu, S., He, B., ... others (2023). Estimating global gpp from the plant functional type perspective using a machine learning approach. *Journal of Geophysical Research: Biogeosciences*, e2022JG007100.

Hadley, N. F., & Szarek, S. R. (1981). Productivity of desert ecosystems. *BioScience*, *31*(10), 747–753.

Harper, K. L., Lamarche, C., Hartley, A., Peylin, P., Ottlé, C., Bastrikov, V., ... others (2022). A 29-year time series of annual 300-metre resolution plant functional type maps for climate models. *Earth System Science Data Discussions*, *2022*, 1–37.

Haslwanter, A., Hammerle, A., & Wohlfahrt, G. (2009). Open-path vs. closed-path eddy covariance measurements of the net ecosystem carbon dioxide and water vapour exchange: A long-term perspective. *Agricultural and Forest Meteorology*, *149*(2), 291-302. Retrieved from https://www.sciencedirect.com/science/article/pii/S0168192308002402 doi: https://doi.org/10.1016/j.agrformet.2008.08.011

Hayek, M. N., Wehr, R., Longo, M., Hutyra, L. R., Wiedemann, K., Munger, J. W., ... Wofsy, S. C. (2018). A novel correction for biases in forest eddy covariance carbon balance. *Agricultural and Forest Meteorology*, *250-251*, 90-101. Retrieved from https://www.sciencedirect.com/science/article/pii/S0168192317306007 doi: https://doi.org/10.1016/j.agrformet.2017.12.186

Hirata, R., Hirano, T., Saigusa, N., Fujinuma, Y., Inukai, K., Kitamori, Y., ... Yamamoto, S. (2007). Seasonal and interannual variations in carbon dioxide exchange of a temperate larch forest. *Agricultural and Forest Meteorology*, *147*(3), 110-124. Retrieved from https://www.sciencedirect.com/science/article/pii/S0168192307001736 doi: https://doi.org/10.1016/j.agrformet.2007.07.005

Ichii, K., Ueyama, M., Kondo, M., Saigusa, N., Kim, J., Alberto, M. C., ... Zhao, F. (2017). New data-driven estimation of terrestrial co2 fluxes in asia using a standardized database of eddy covariance measurements, remote sensing data, and support vector regression. *Journal of Geophysical Research: Biogeosciences*, *122*(4), 767-795. Retrieved from https://agupubs.onlinelibrary.wiley.com/doi/abs/10.1002/2016JG003640 doi: https://doi.org/10.1002/2016JG003640

Jung, M., Koirala, S., Weber, U., Ichii, K., Gans, F., Camps-Valls, G., ... Reich-

stein, M. (2019). The fluxcom ensemble of global land-atmosphere energy fluxes. *Scientific data*, *6*(1), 74.
Jung, M., Schwalm, C., Migliavacca, M., Walther, S., Camps-Valls, G., Koirala, S., ... Reichstein, M. (2020). Scaling carbon fluxes from eddy covariance sites to globe: synthesis and evaluation of the fluxcom approach. *Biogeosciences*, *17*(5), 1343–1365. Retrieved from https://bg.copernicus.org/articles/17/1343/2020/ doi: 10.5194/bg-17-1343-2020
Kämäräinen, M., Tuovinen, J.-P., Kulmala, M., Mammarella, I., Aalto, J., Vekuri, H., ... Lintunen, A. (2023). Spatiotemporal lagging of predictors improves machine learning estimates of atmosphere–forest co_2 exchange. *Biogeosciences*, *20*(4), 897–909. Retrieved from https://bg.copernicus.org/articles/20/897/2023/ doi: 10.5194/bg-20-897-2023
Köhler, P., Frankenberg, C., Magney, T. S., Guanter, L., Joiner, J., & Landgraf, J. (2018). Global retrievals of solar-induced chlorophyll fluorescence with tropomi: First results and intersensor comparison to oco-2. *Geophysical Research Letters*, *45*(19), 10–456.
Le Quéré, C., Andrew, R. M., Friedlingstein, P., Sitch, S., Hauck, J., Pongratz, J., ... others (2018). Global carbon budget 2018. *Earth System Science Data Discussions*, *2018*, 1–3.
Li, X., Xiao, J., He, B., Altaf Arain, M., Beringer, J., Desai, A. R., ... Varlagin, A. (2018). Solar-induced chlorophyll fluorescence is strongly correlated with terrestrial photosynthesis for a wide variety of biomes: First global analysis based on oco-2 and flux tower observations. *Global Change Biology*, *24*(9), 3990-4008. Retrieved from https://onlinelibrary.wiley.com/doi/abs/10.1111/gcb.14297 doi: https://doi.org/10.1111/gcb.14297
Lin, S., Li, J., Liu, Q., Gioli, B., Paul-Limoges, E., Buchmann, N., ... others (2021). Improved global estimations of gross primary productivity of natural vegetation types by incorporating plant functional type. *International Journal of Applied Earth Observation and Geoinformation*, *100*, 102328.
Liu, X., Liu, L., Hu, J., Guo, J., & Du, S. (2020). Improving the potential of red sif for estimating gpp by downscaling from the canopy level to the photosystem level. *Agricultural and Forest Meteorology*, *281*, 107846.
Madani, N., Kimball, J. S., Jones, L. A., Parazoo, N. C., & Guan, K. (2017). Global analysis of bioclimatic controls on ecosystem productivity using satellite observations of solar-induced chlorophyll fluorescence. *Remote Sensing*, *9*(6). Retrieved from https://www.mdpi.com/2072-4292/9/6/530 doi: 10.3390/rs9060530
Madani, N., Kimball, J. S., Parazoo, N. C., Ballantyne, A. P., Tagesson, T., Jones, L. A., ... Geruo, A. (2020, mar). Below-surface water mediates the response of african forests to reduced rainfall. *Environmental Research Letters*, *15*(3), 034063. Retrieved from https://dx.doi.org/10.1088/1748-9326/ab724a doi: 10.1088/1748-9326/ab724a
Montgomery, R. A., & Chazdon, R. L. (2001). Forest structure, canopy architecture, and light transmittance in tropical wet forests. *Ecology*, *82*(10), 2707–2718.
Muñoz Sabater, J. (2019). *ERA5-Land hourly data from 1950 to present.* Copernicus Climate Change Service (C3S) Climate Data Store (CDS). Retrieved from https://doi.org/10.24381/cds.e2161bac doi: 10.24381/cds.adbb2d47
Myneni, R., Knyazikhin, Y., & Park, T. (2021). *MODIS/Terra leaf area Index/FPAR 8-day L4 global 500m SIN grid V061.* NASA EOSDIS Land Processes Distributed Active Archive Center.
Nathaniel, J., Liu, J., & Gentine, P. (2023). Metaflux: Meta-learning global carbon fluxes from sparse spatiotemporal observations. *Scientific Data*, *10*(1), 440.
Norton, A. J., Rayner, P. J., Koffi, E. N., Scholze, M., Silver, J. D., & Wang, Y.-P. (2019). Estimating global gross primary productivity using chlorophyll fluorescence and a data assimilation system with the bethy-scope model. *Bio-*

geosciences, *16*(15), 3069–3093.

Palmer, P. I., Wainwright, C. M., Dong, B., Maidment, R. I., Wheeler, K. G., Gedney, N., . . . others (2023). Drivers and impacts of eastern african rainfall variability. *Nature Reviews Earth & Environment*, *4*(4), 254–270.

Pan, Y., Birdsey, R. A., Fang, J., Houghton, R., Kauppi, P. E., Kurz, W. A., . . . others (2011). A large and persistent carbon sink in the world's forests. *Science*, *333*(6045), 988–993.

Pastorello, G., Trotta, C., Canfora, E., Chu, H., Christianson, D., Cheah, Y.-W., . . . others (2020). The fluxnet2015 dataset and the oneflux processing pipeline for eddy covariance data. *Scientific data*, *7*(1), 225.

Phan, A., & Fukui, H. (2023, December). *FluxFormer: Upscaled Global Carbon Fluxes from Eddy Covariance Data with Multivariate Timeseries Transformer.* Zenodo. Retrieved from `https://doi.org/10.5281/zenodo.13949006` doi: 10.5281/zenodo.13949006

Piao, S., Wang, X., Park, T., Chen, C., Lian, X., He, Y., . . . others (2020). Characteristics, drivers and feedbacks of global greening. *Nature Reviews Earth & Environment*, *1*(1), 14–27.

Poulter, B., Ciais, P., Hodson, E., Lischke, H., Maignan, F., Plummer, S., & Zimmermann, N. (2011). Plant functional type mapping for earth system models. *Geoscientific Model Development*, *4*(4), 993–1010.

Poulter, B., Frank, D., Ciais, P., Myneni, R. B., Andela, N., Bi, J., . . . others (2014). Contribution of semi-arid ecosystems to interannual variability of the global carbon cycle. *Nature*, *509*(7502), 600–603.

Poulter, B., MacBean, N., Hartley, A., Khlystova, I., Arino, O., Betts, R., . . . others (2015). Plant functional type classification for earth system models: results from the european space agency's land cover climate change initiative. *Geoscientific Model Development*, *8*(7), 2315–2328.

Runge, J., Bathiany, S., Bollt, E., Camps-Valls, G., Coumou, D., Deyle, E., . . . Zscheischler, J. (2019, Jun 14). Inferring causation from time series in earth system sciences. *Nature Communications*, *10*(1), 2553. Retrieved from `https://doi.org/10.1038/s41467-019-10105-3` doi: 10.1038/s41467-019-10105-3

Runge, J., Gerhardus, A., Varando, G., Eyring, V., & Camps-Valls, G. (2023, Jul 01). Causal inference for time series. *Nature Reviews Earth & Environment*, *4*(7), 487-505. Retrieved from `https://doi.org/10.1038/s43017-023-00431-y` doi: 10.1038/s43017-023-00431-y

Sanders, A. F., Verstraeten, W. W., Kooreman, M. L., Van Leth, T. C., Beringer, J., & Joiner, J. (2016). Spaceborne sun-induced vegetation fluorescence time series from 2007 to 2015 evaluated with australian flux tower measurements. *Remote Sensing*, *8*(11), 895.

Seneviratne, S., Nicholls, N., Easterling, D., Goodess, C., Kanae, S., Kossin, J., . . . Zhang, X. (2012, 04). Changes in climate extremes and their impacts on the natural physical environment. In C. Field et al. (Eds.), (Vol. Managing the Risks of Extreme Events and Disasters to Advance Climate Change Adaptation, p. 109-230). Cambridge University Press, Cambridge, UK, and New York, NY, USA. (A Special Report of Working Groups I and II of the Intergovernmental Panel on Climate Change (IPCC))

Shekhar, A., Buchmann, N., & Gharun, M. (2022). How well do recently reconstructed solar-induced fluorescence datasets model gross primary productivity? *Remote Sensing of Environment*, *283*, 113282. Retrieved from `https://www.sciencedirect.com/science/article/pii/S0034425722003881` doi: https://doi.org/10.1016/j.rse.2022.113282

Sitch, S., Friedlingstein, P., Gruber, N., Jones, S. D., Murray-Tortarolo, G., Ahlström, A., . . . others (2015). Recent trends and drivers of regional sources and sinks of carbon dioxide. *Biogeosciences*, *12*(3), 653–679.

Tramontana, G., Jung, M., Schwalm, C. R., Ichii, K., Camps-Valls, G., Ráduly, B., . . . others (2016). Predicting carbon dioxide and energy fluxes across global fluxnet sites with regression algorithms. *Biogeosciences*, *13*(14), 4291–4313.

Vaswani, A., Shazeer, N., Parmar, N., Uszkoreit, J., Jones, L., Gomez, A. N., . . . Polosukhin, I. (2017). Attention is all you need. *Advances in neural information processing systems*, *30*.

Wang, S., Zhang, Y., Ju, W., Qiu, B., & Zhang, Z. (2021). Tracking the seasonal and inter-annual variations of global gross primary production during last four decades using satellite near-infrared reflectance data. *Science of The Total Environment*, *755*, 142569. Retrieved from `https://www.sciencedirect.com/science/article/pii/S0048969720360988` doi: https://doi.org/10.1016/j.scitotenv.2020.142569

Wu, H., Xu, J., Wang, J., & Long, M. (2021). Autoformer: Decomposition transformers with auto-correlation for long-term series forecasting. *Advances in Neural Information Processing Systems*, *34*, 22419–22430.

Xiao, J., Li, X., He, B., Arain, M. A., Beringer, J., Desai, A. R., . . . others (2019). Solar-induced chlorophyll fluorescence exhibits a universal relationship with gross primary productivity across a wide variety of biomes. *Global change biology*, *25*(4), e4–e6.

Xu, L., Saatchi, S. S., Yang, Y., Myneni, R. B., Frankenberg, C., Chowdhury, D., & Bi, J. (2015). Satellite observation of tropical forest seasonality: spatial patterns of carbon exchange in amazonia. *Environmental Research Letters*, *10*(8), 084005.

Yan, P., He, N., Yu, K., Xu, L., & Van Meerbeek, K. (2023). Integrating multiple plant functional traits to predict ecosystem productivity. *Communications Biology*, *6*(1), 239.

Yang, H., Yang, X., Zhang, Y., Heskel, M. A., Lu, X., Munger, J. W., . . . Tang, J. (2017). Chlorophyll fluorescence tracks seasonal variations of photosynthesis from leaf to canopy in a temperate forest. *Global Change Biology*, *23*(7), 2874–2886.

Yang, R., Wang, J., Zeng, N., Sitch, S., Tang, W., McGrath, M. J., . . . others (2022). Divergent historical gpp trends among state-of-the-art multi-model simulations and satellite-based products. *Earth System Dynamics*, *13*(2), 833–849.

Zeng, J., Matsunaga, T., Tan, Z.-H., Saigusa, N., Shirai, T., Tang, Y., . . . Fukuda, Y. (2020). Global terrestrial carbon fluxes of 1999–2019 estimated by upscaling eddy covariance data with a random forest. *Scientific data*, *7*(1), 313.

Zerveas, G., Jayaraman, S., Patel, D., Bhamidipaty, A., & Eickhoff, C. (2021). A transformer-based framework for multivariate time series representation learning. In *Proceedings of the 27th acm sigkdd conference on knowledge discovery & data mining* (pp. 2114–2124).

Zhang, Y., Guanter, L., Berry, J. A., van der Tol, C., Yang, X., Tang, J., & Zhang, F. (2016). Model-based analysis of the relationship between sun-induced chlorophyll fluorescence and gross primary production for remote sensing applications. *Remote Sensing of Environment*, *187*, 145–155.

Zhang, Y., Xiao, X., Wu, X., Zhou, S., Zhang, G., Qin, Y., & Dong, J. (2017, Oct 24). A global moderate resolution dataset of gross primary production of vegetation for 2000–2016. *Scientific Data*, *4*(1), 170165. Retrieved from `https://doi.org/10.1038/sdata.2017.165` doi: 10.1038/sdata.2017.165

Zhang, Z., Ju, W., Li, X., Cheng, X., Zhou, Y., Xu, S., . . . Li, J. (2024). Joint improvement on absorbed photosynthetically active radiation and intrinsic quantum yield efficiency algorithms in the p model betters the estimate of terrestrial gross primary productivity. *Agricultural and Forest Meteorology*, *346*, 109883. Retrieved from `https://www.sciencedirect.com/science/article/pii/S0168192323005737` doi: https://doi.org/10.1016/

j.agrformet.2023.109883
Zhang, Z., Zhang, Y., Porcar-Castell, A., Joiner, J., Guanter, L., Yang, X., ... Goulas, Y. (2020). Reduction of structural impacts and distinction of photosynthetic pathways in a global estimation of gpp from space-borne solar-induced chlorophyll fluorescence. *Remote Sensing of Environment*, *240*, 111722. Retrieved from `https://www.sciencedirect.com/science/article/pii/S0034425720300912` doi: https://doi.org/10.1016/j.rse.2020.111722
Zhou, H., Zhang, S., Peng, J., Zhang, S., Li, J., Xiong, H., & Zhang, W. (2021). Informer: Beyond efficient transformer for long sequence time-series forecasting. In *Proceedings of the aaai conference on artificial intelligence* (Vol. 35, pp. 11106–11115).
Zhou, T., Ma, Z., Wen, Q., Wang, X., Sun, L., & Jin, R. (2022). Fedformer: Frequency enhanced decomposed transformer for long-term series forecasting. In *International conference on machine learning* (pp. 27268–27286).